SAGE Publishing

Research Article

Ultrahigh Adsorption Capacity Zirconium-Magnesium Composite Oxide Nanoclusters Remove Malachite Green from Aqueous Media

Yulong Sun,[1] Haoxin Zheng,[2] Yanfeng Pu,[1] Hao Yang [ID],[1] Jianhong Wang [ID],[1] Shuaishuai Zhou,[1] Qian Li,[1] and Congzhen Qiao[1]

[1]College of Chemistry and Chemical Engineering, Henan Province Engineering Research Center of Catalytic Reaction, Henan University, Kaifeng, China 475004
[2]Shenzhen Academy of Environmental Science, Shenzhen, China 518000

Correspondence should be addressed to Hao Yang; hyang@henu.edu.cn and Jianhong Wang; jhwnj@163.com

The environmental pollution caused by organic dyes has damaged serious harm to human life. Hence, a series of Zr-Mg composite oxide nanoclusters with different metal ratios were synthesized by solvothermal method for adsorption of malachite green in aqueous solution. The optimal adsorbent with Zr/Mg metal molar ratio of 1 : 2 presented good adsorption performance, which adsorption capacity reached 12647.60 mg/g, and removal rate of malachite green reached more than 99%. These adsorbents were characterized by X-ray diffraction, Fourier-transform infrared spectra, nitrogen adsorption-desorption, scanning electron microscope, transmission electron microscope, and other methods. Influence of initial concentration of malachite green solution, pH, adsorption temperature, and contact time on absorption efficiency was investigated through batch experiments. Pseudo-second-order kinetic model can well describe the adsorption kinetic data. The three-parameter Sips isotherm model was more suitable for predicting the experimental results than Langmuir and Freundlich, and the adsorption process was endothermic.

1. Introduction

Along with the needs of human productive activities, the application of dyes in various industries is becoming more and more wide, especially in the textile, leather, paper, plastic, and other industries [1, 2] with the largest application demand. It brings rich colors to human life, but the discharge of dye wastewater into the ecosystem will lead to eutrophication [3] and discoloration [4] of water bodies, which will destroy the ecosystem. It will also pose a threat to human health, with the risk of carcinogenic, teratogenic, and mutagenic [5]. Malachite green (MG) is a typical synthetical triphenylmethane organic compounds, which is not only a common dye but also as an effective fungicide and insecticide [6, 7]. While MG has the characteristics of high toxicity and residue [8] in human body, it will also cause different degrees of damage to the respiratory system, eyes, skin tissue, etc. Therefore, reducing the pollution is not only achieving the goal of protecting the environment but also an effective measure to defend human health.

Like other organic dyes, MG is soluble in water and stable, and it is difficult to achieve effective treatment of dye wastewater pollution in a short time depending on the purification capacity of natural ecosystem. At present, physical or chemical methods such as reverse osmosis, ion exchange, photocatalysis, electrolysis, and filtration [5, 9, 10] technology have been applied to treat dye wastewater. These technologies show explicit advantages, but adsorption is regarded as an effective process method to treat dye wastewater due to its simple operation, low cost, wide material sources, and degradation depth [11–13]. Among the numerous adsorbents, metal oxide adsorbents possess rich adsorption sites, strong chemical stability, high point of zero charge, and crystallinity, meanwhile they are environmentally friendly

[14, 15]. Compared with single metal oxide adsorbents, composite metal oxide adsorbents have better adsorption capacity, anisotropy, good mechanical stability, big surface area, and pore volume are part of the reason for its degradation ability [16].

Over the past few decades, zirconium-based composite materials were widely applied in water treatment field in various forms. This is because the introduction of zirconium improved the adsorbent properties such as large specific surface area and pore volume [17], improved physical and chemical stability, plentiful adsorption sites [18], and low diffusion resistance [19–22]. As an alkaline earth metal, magnesium is a wide application in many fields; it also shows good performance in the field of environmental governance. According to the previous studies, it was found that the introduction of magnesium could increase the adsorption capacity of the material for different dyes [23–26]. Renuka et al. [27] prepared Mg doped ZrO_2 nanoparticles by Aloe Vera gel assisted method to degraded Rhodamine B. However, Zirconium-magnesium composite materials have excellent heat resistance and corrosion resistance, and are widely used in industries such as manufacturing high temperature nozzles and steam turbine blades [28], and there are few reports in the field of environmental governance.

In this study, we synthesized a zirconium-magnesium composite oxide nanocluster with ultrahigh adsorption capacity. Firstly, MG removal performance, kinetics, and isotherms were evaluated to obtain an optimized composition of Zr/Mg molar ratio and pH of MG solution. Then, various technologies were used to characterize the prepared adsorbents in order to analyze their surface, morphology, and structural characteristics. Additionally, the reusability of the nanocluster after desorption was evaluated. Finally, the adsorption mechanism was demonstrated by employing characterization techniques. With the aforementioned results, this study is aimed at suggesting an economic, high adsorption, and efficient adsorbent for MG removal.

2. Materials and Methods

2.1. Chemicals for Synthesis.
Malachite green ($C_{52}H_{54}N_4O_{12}$, AR, $\lambda_{max} = 617$ nm)was purchased from Macklin company. Zirconium nitrate pentahydrate ($Zr(NO_3)_4 \bullet 5H_2O$, ≥99.0%) and magnesium nitrate hexahydrate ($Mg(NO_3)_2 \bullet 6H_2O$, ≥99.0%), KOH (≥96.0%), HCl (36–38%) were obtained from Tianjin Kermel Chemical Reagents Co., LTD. (Tianjin, China) and Sinopharm Chemical Reagents Co., LTD. (Shanghai, China), respectively. Anhydrous ethanol was bought from Tianjin Fuyu Fine Chemicals Co., LTD. (Tianjin, China) and KCl (≥99.5%) from Tianjin Tianda Chemical Experiment Factory. All reagents were directly used without further purification in this study.

2.2. Preparation of Zr-Mg Composite Oxide Nanoclusters.
Zr-Mg composite oxide nanoclusters were prepared by solvothermal method [29]. 7.2 mmol $Zr(NO_3)_4$ 5H$_2$O and x mol (x = 3.6, 5.4, 7.2, 9.0, 10.8, 12.6, 14.4) $Mg(NO_3)_2 \bullet 6H_2O$ were dissolve in 40 mL anhydrous ethanol. The solution was stirred for 30 min after dissolution completely. Then, 40 mL 4 M sodium hydroxide aqueous solution of ethanol was added dropwise in 90 min and stirred for 1 h. The mixture was transferred into an autoclave with Telfon liner, heated at 120°C for 12 h. After natural cooling, the solid sample was washed by deionized water until it was natural. The sample was dried for 8 h at 60°C and calcined at 700°C to obtain the adsorbent, which was denoted as y-ZM (y: the molar ratio of Mg/Zr, ZM: Zr-Mg composite oxide). Likewise, pure ZrO_2 and MgO were prepared in the same way. The schematic diagram of the adsorbents was displayed in Scheme 1.

2.3. Characterization.
X-ray Diffraction (XRD) analyses were obtained from Bruker D8 Advance (Bruker, Germany) from 5° to 90° with Cu Kα radiation ($\lambda = 1.5406$ Å). Fourier transform infrared (FT-IR) spectra carried out Bruker Vertex 70 spectrometer (Bruker, Germany) scan with a range of 400-4000 cm^{-1}. The Autosorb-iQ-MP-C (Quantachrome, American) was employed to determine nitrogen adsorption-desorption isotherm, specific surface area and pore volume were calculated by Brunauer-Emmett-Teller (BET) method; pore size distribution was calculated by Barrett-Joyner-Halenda (BJH) method. The morphology of the samples was analyzed by field emission scanning electron microscope (FESEM) (JEOL JSM-7610F Plus, Japan), and field emission transmission electron microscope (FETEM) JEOL JEM-F200, Japan) with an energy dispersive spectrometer (EDS). The X-ray photoelectron spectroscopy (XPS) was carried out by X-ray diffractometer (ESCALAB250Xi, Thermo Fisher Scientific, American) with Al Kα radiation, C1s binding energy (BE) at 284.8 eV was referenced. pH at the point of zero charge (pH$_{PZC}$) was determined as follows [30, 31]. A series of initial pH (pH$_{initial}$) from 2 to 12 was adjusted by 0.1 M HCl and 0.1 M KOH. Then, 50 mL KCl solution (0.1 M) with different pH was added to a flask containing 20 mg adsorbent, and the final pH (pH$_{final}$) was measured after stirring for 48 h. pH$_{initial}$ and pH$_{final}$ were used to calculate the pH$_{PZC}$.

2.4. Batch Adsorption Experiments.
The 5000 mg/L MG solution was prepared as stock solution, and a certain amount of MG stock solution was diluted to the desired concentration at each experiment. Batch adsorption tests were carried out in sealed conical bottles containing 50 mL MG solution in an air shaker (THZ-100, Shanghai Yiheng Instrument Co., LTD., Shanghai, China). The effects of temperature (303 K, 313 K, and 323 K), initial solution concentration (1000-5000 mg/L), pH [2–7] of MG solution, and time on the adsorption were investigated. The concentration of MG solution was analyzed via a dual-beam UV-Vis spectrophotometer ($\lambda_{max} = 617$ nm, length of cell = 1.0 cm, PERSEE TU-1900, Beijing, China). The adsorption performance of adsorbents for MG were described by q_e (mg/g) and removal rate, it can be calculated as follows:

$$q_e = \frac{(c_0 - c_e)V}{m},\qquad(1)$$
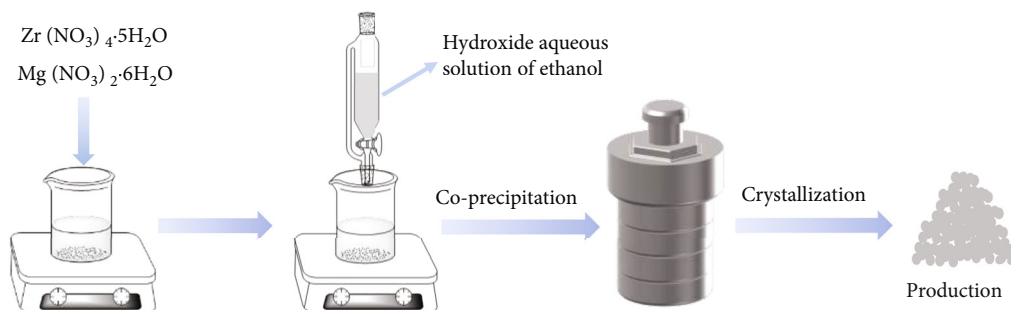
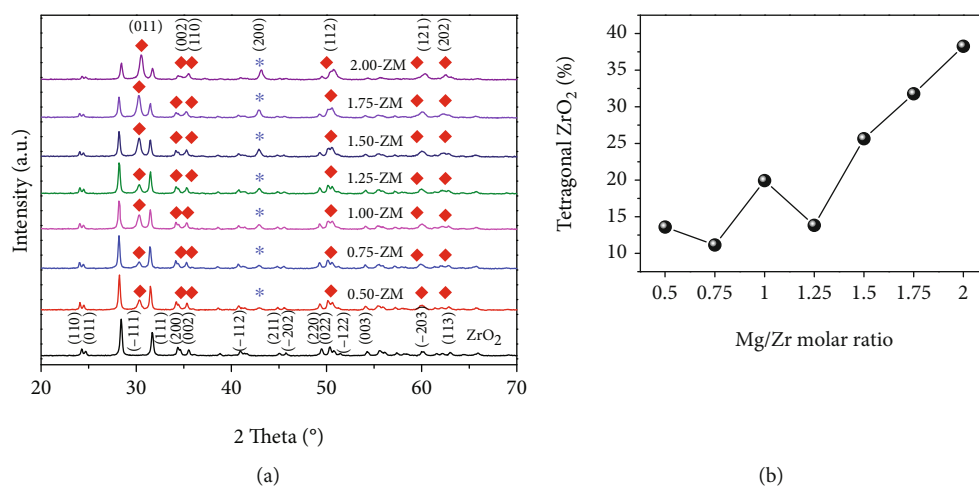SCHEME 1: Schematic representation of y-ZM synthesis procedure.

(a)

(b)

FIGURE 1: (a) XRD patterns for y-ZM samples and (b) percentage of t-ZrO$_2$ present at different Mg/Zr molar ratio.

$$\text{Removal rate (\%)} = \frac{c_0 - c_e}{c_0} * 100, \qquad (2)$$

where m (g) is the adsorbent dose, q_e (mg/g) is the equilibrium absorption capacity, V (mL) is the MG solution volume, and c_0 and c_e (mg/L) are the initial and equilibrium MG solution concentration, respectively.

3. Results and Discussion

3.1. Characterization of y-ZM. Figure 1(a) shows the XRD pattern of y-ZM (y=0.50-2.00) and pure ZrO$_2$. According to Figure 1(a), pure ZrO$_2$ presented in all y-ZMs in the form of monoclinic phase (PDF#37-1484, m-ZrO$_2$). The planes (-111) and (111) corresponding two strong diffraction peaks at 28.2° and 31.5° belong to m-ZrO$_2$. Two strong diffraction peaks at 30.3° and 50.4° belonged to tetragonal zirconia (PDF#50-1089, t-ZrO$_2$), and the corresponding planes were (011) and (112), respectively. The diffraction peak at 42.9° and its corresponding (200) plane was cubic phase of magnesium oxide (PDF#45-0946), and the intensity of this peak increased with the increase of magnesium abundance. It can be seen from the Figure 1(a) that intensity of the diffraction peak of t-ZrO$_2$ at 30.3° showed an increase trend with increase of magnesium abundance. Due to a large number oxygen vacancies in MgO [27], m-ZrO$_2$ will exhibit a tendency transform to tetragonal phase [19]. Therefore, the content of t-ZrO$_2$ in the adsorbents of y-ZM rises with the increasing of magnesium abundance, which caused the intensity of diffraction peak of t-ZrO$_2$ at 30.3°.

The fraction of t-ZrO$_2$ in the mixture phase of ZrO$_2$ (t-ZrO$_2$ and m-ZrO$_2$) was calculated by

$$X_t = \frac{1 - R}{1 + 0.311R}, \qquad (3)$$

$$R = \frac{I_m(-111) + I_m(111)}{I_m(-111) + I_m(111) + I_t(011)}, \qquad (4)$$

where I is the integrate intensity of the XRD line.

Figure 1(b) indicated the abundance of tetragonal phase relative to the monoclinic phase obtained from the analysis. This also showed that the content of t-ZrO$_2$ phase increased with increase in Mg^{2+} concentration. It indicated that at 700°C, the concentration of oxygen vacancies increases due to the presence of Mg^{2+}, and the m-ZrO$_2$ needed to transform to the t-ZrO$_2$ to maintain the stability of the material [32]. Changes of oxygen content can also cause phase transition of ZrO$_2$ [28, 33], the low diffraction peaks intensity of 0.75-ZM and 1.25-ZM at 30.3° may be caused by the lower oxygen content in the calcination process.

XPS analysis of 2.00-ZM was applied to evaluate the element composition and oxidation state, and the results were presented in Figure 2 and Figure S4. The characteristic
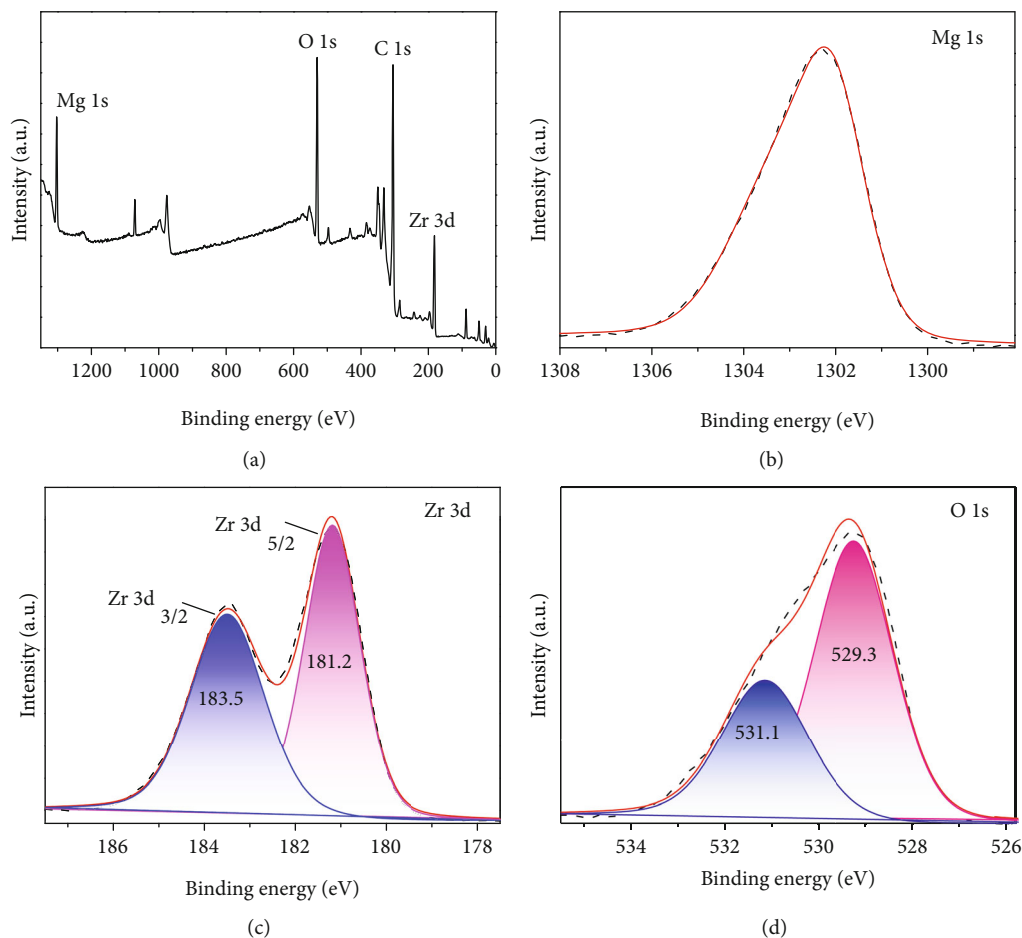
(a)

(b)

(c)

(d)

Figure 2: (a) XPS survey spectrum, (b) high-resolution spectra of Mg1s, Zr3d (c), and (d) O1s on the 2.00-ZM adsorbent surface.
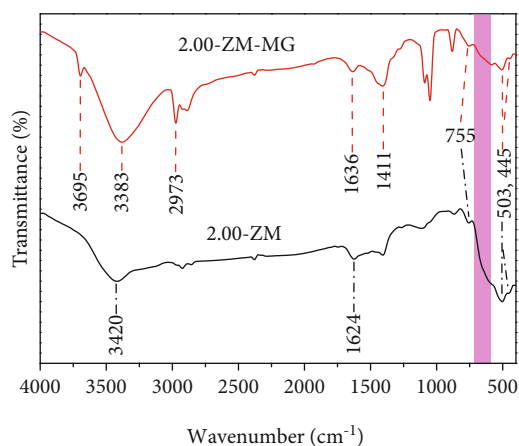

Figure 3: FT-IR spectrums of 2.00-ZM (before the adsorption) and MG/2.00-ZM (after the adsorption).

peaks of Mg, Zr, C, and O elements can be observed in Figure 2(a). Mg 1 s (Figure 2(b)) spectrum fitted by 1302.5, which was in accord with previously reported in the literature for Mg^{2+}[26]. Zr $3d_{3/2}$ at 183.5 eV and Zr $3d_{5/2}$ at 181.2 eV constituted the Zr 3d spectrum (Figure 2(c)). It

was reported that the BE of pure ZrO_2 Zr $3d_{3/2}$ and Zr $3d_{5/2}$ is 183.9 and 181.6 eV, respectively, and the BE decreased in this work due to the strong electrophilicity of ZrO_2 [34]. The high-resolution O 1 s spectrum (Figure 2(d)) of 2.00-ZM was divided into two peaks by deconvolution. The BE was concentrated at 529.3 and 531.1 eV, respectively, corresponding to the lattice oxygen in the sample and hydroxyl groups on the surface [27, 35].

Figure 3 was the FT-IR spectrum of 2.00-ZM before and after adsorption. The peaks at 445 and 755 cm^{-1} corresponding to the Zr-O stretching vibration of monoclinic ZrO_2, 503 cm^{-1} was the Zr-O stretching vibration of tetragonal ZrO_2 [32, 36]. The transmittance enhancement of the broad peak at 1411 cm^{-1} may be caused by the C=C stretching vibration in the benzene ring of MG. The Mg-O-Mg vibration modes of MgO [37] appeared between 750 cm^{-1} and 583 cm^{-1}. The peak at 1624 cm^{-1} and 3420 cm^{-1} was due to H-O-H bending vibration and stretching vibration of -OH of adsorbed water, respectively [9, 38]. The peaks at 1624 cm^{-1} and 3420 cm^{-1} were shifted a little from the spectrum of 2.00-ZM after adsorption, which was caused by the adsorption of MG on 2.00-ZM. The peak at 3695 cm^{-1} was due to the stretching vibration of free -OH [39].

Figure 4(a) and Figure S1(a) showed that the pure MgO mainly exists in three shapes, they existed in the forms of
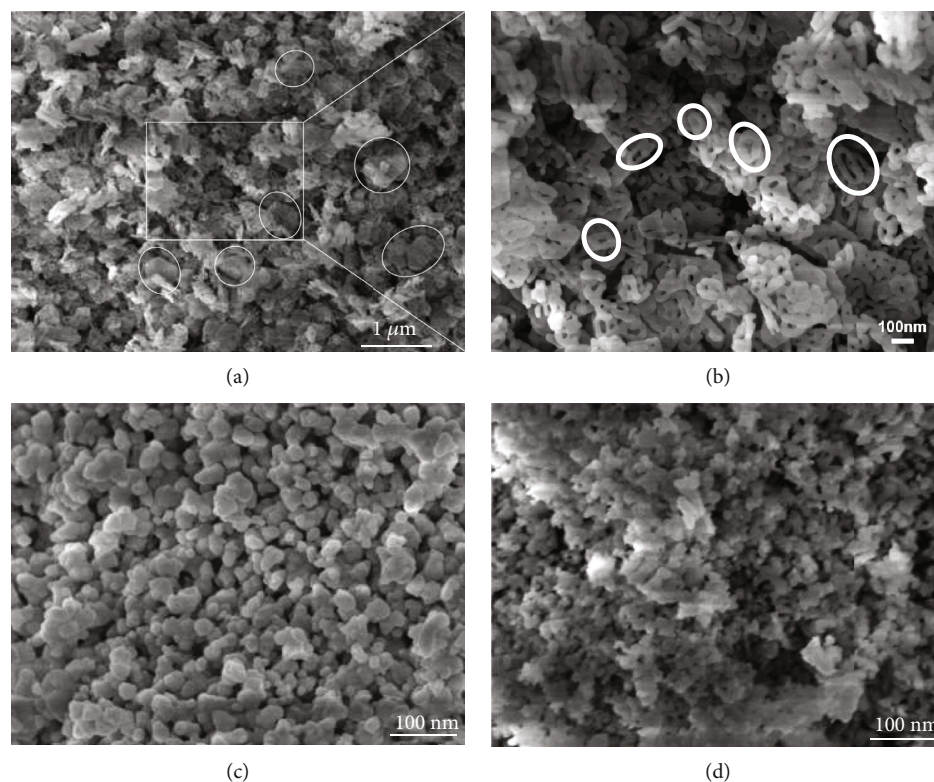
(a)

(b)

(c)

(d)

FIGURE 4: FESEM images of (a, b) pure MgO, (c) pure ZrO$_2$, and (d) 2.00-ZM.

regular quadrilateral and hexagonal, and irregular net-like shapes, respectively. These net-like structures were self-assembled from the open loop as shown in Figure 4(b) and Figure S1(b) as basic units. The self-assembled of these basic units developed into a single-loop, double-loop, irregular network shape as shown in Figure S1(c–e), and finally become a hexagonal shape as shown in Figure S1(a). The size and shape of pure ZrO$_2$ (Figure 4(c) and Figure S2) were not uniform, there were not only spheres around 30 nm but also clusters mainly existed around 200 nm. Figures 4(d) and 5(a) show that the 2.00-ZM composite metal oxides inherited the morphology of ZrO$_2$ clusters and the clusters size were basically around 200 nm. These clusters of 2.00-ZM assembled by about 30 nm spheres were beneficial to increase the number of intergranular mesoporous and facilitate the adsorption of MG on the surface of adsorbents.

Further characterization to the structure of the 2.00-ZM clusters were carried out by TEM, high-angular-annular dark field scanning transmission electron microscopy (HAADF-STEM, Figure 5(b)), and EDS, high-resolution transmission electron microscopy (HR-TEM). Figures 5(c)–5(g) demonstrate the elemental EDS mapping results of 2.00-ZM clusters, confirming the elements of Zr, Mg, and O existed in the prepared 2.00-ZM clusters. Mg exhibited the same contour with O, but distribution of Mg and Zr in some areas is different. This is because the magnesium ions in the divalent cationic state have difficulty getting into the crystal lattice of zirconia

[27]. It can be seen that clear lattice fringe from the HR-TEM image shown in Figure 5(h) indicated that the as-prepared samples presented a crystal conformation in nature. The measured lattice spacing is 0.2905 nm, which correspond well to the (011) plane of t-ZrO$_2$, and further explained the existence of tetragonal zirconia.

Figure S3 were presented nitrogen adsorption-desorption isotherms and pore size distribution for y-ZM, and the corresponding structural parameters were listed in Table 1. According to IUPAC classification, these isotherms belong to type II and type IV isotherms. The relative pressure rose smoothly between 0.2 and 0.8 because of multilayer adsorption of N$_2$ molecules on the surface of the adsorbents, and rapidly rose between 0.8 and 1.0 is due to occurrence of capillary condensation [32]. From Figure S3(b), existence of adsorption hysteresis indicated that the series of y-ZM were mesoporous materials [40]. It can be seen from Table 1, with the increase of magnesium abundance (y increased from 0.50 to 2.00), V$_t$ and D$_{ave}$ of the samples gradually increase (V$_t$ increased from 28.697 m [2]/g to 34.550 m [2]/g, D$_{ave}$ increased from 2.152 nm to 3.708 nm), which can effectively reduce the diffusion resistance and enhance the adsorption rate of dye. But, with the increase of magnesium abundance, S$_{BET}$ showed an increasing trend. It can be concluded that the abundance of Mg was the dominant factor causing the increase of pore volume and surface, and the adsorption capacity of the adsorbents may increase with the abundance of Mg.
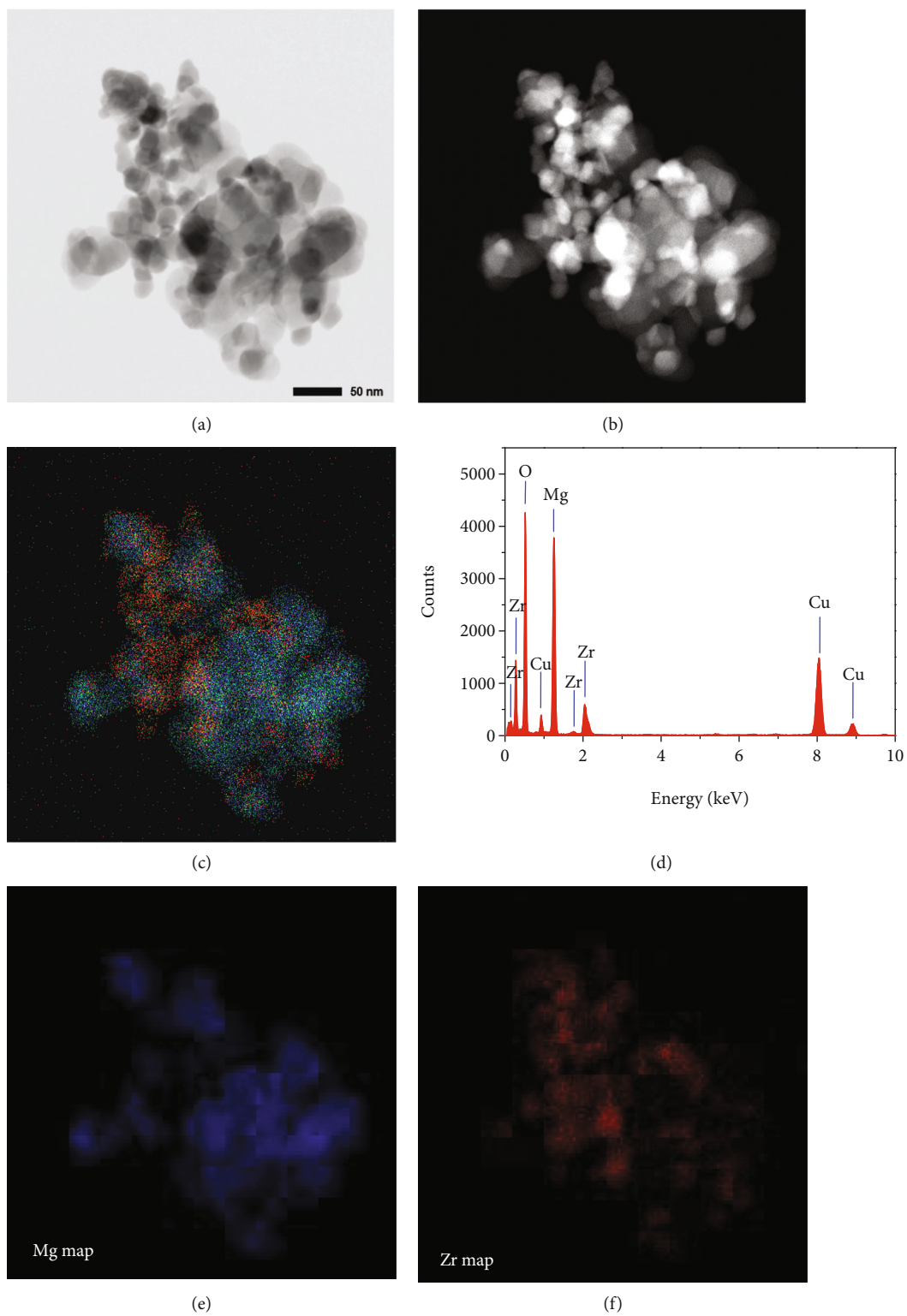
(a)

(b)

(c)

(d)
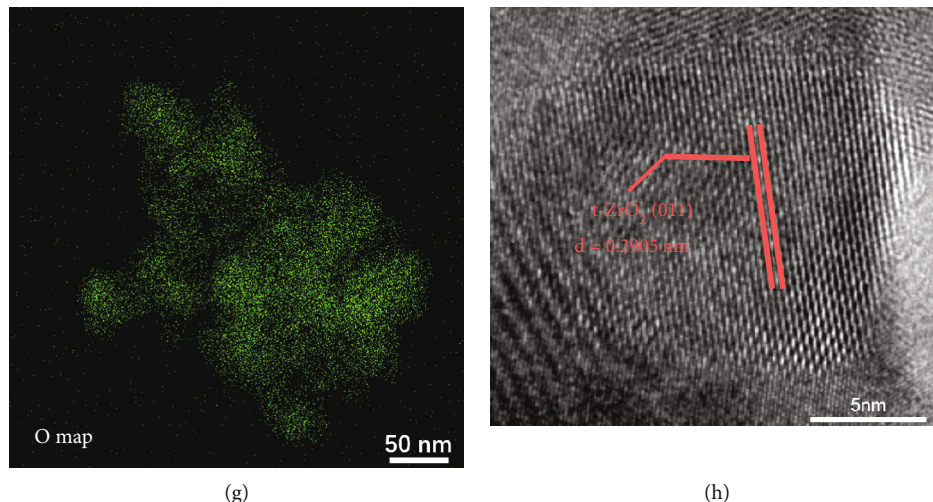

(e)

(f)

Figure 5: Continued.

(g)

(h)

FIGURE 5: TEM (a) and HAADF-STEM (b) images of 2.00-ZM clusters; EDS analysis of the clusters (d); elemental mapping images of the clusters (c) and (e–g); HR-TEM image of the clusters.

TABLE 1: Detailed properties of y-ZM obtained from BET and BJH method (S_{BET}: specific surface area; V_t: total pore volume; D_{ave}: average pore diameter).

Sample	S_{BET} (m^2/g)	V_t (cm^3/g)	D_{ave} (nm)
0.50-ZM	28.697	0.154	2.152
0.75-ZM	25.962	0.188	2.892
1.00-ZM	16.046	0.219	5.448
1.25-ZM	30.803	0.237	3.082
1.50-ZM	34.881	0.288	3.307
1.75-ZM	33.489	0.307	3.665
2.00-ZM	34.550	0.320	3.708

3.2. Determination of the Optimal Adsorbent. In order to determine the optimal Zr/Mg molar ratio, a series of y-ZM NPs with different Mg abundances were investigated as adsorbents for MG removal. From Figure 6, it can be seen that with the increase of "y", the adsorption capacity of y-ZM for MG also increased. This may be because pore volume played a key role in the adsorption process, it can be seen from Table 1 that the adsorption capacity of y-ZM showed a positive relationship with the pore volume, which make the diffusion resistance effectively reduced. For this reason, the adsorption capacity of y-ZM increased with the increase of abundance of Mg. Therefore, the optimal Zr/Mg molar ratio is 4 : 8.

3.3. Determination of pH_{PZC} and the pH Effect on MG Adsorption by 2.00-ZM. The pH_{PZC} of 2.00-ZM is shown in Figure 6(b) and the value was 11.02, which may indicate that the MG removal with 2.00-ZM was more effective at pH > 3.00. As shown in Figure 6(c), the experimental results were as expected, and the removal rate of 2.00-ZM for MG in solution can reach more than 99% when pH ≥ 3. However, removal rate of MG at initial pH of 2 is only about 10%, which may due to the competitive adsorption of excess H^+ with $C_{23}H_{25}N_2^+$ in the solution [41]. The H^+ adsorbed on the surface of 2.00-ZM causes protonation (Figure 7),

which reduced the adsorption capacity of 2.00-ZM to $C_{23}H_{25}N_2^+$ due to electrostatic repulsion. The deprotonation of the 2.00-ZM surface makes it maintain negative charge and enhanced the removal of $C_{23}H_{25}N_2^+$ when the pH was greater than 2. Moreover, due to the existence of C=C and C-N bonds in $C_{23}H_{25}N_2^+$, $\pi - \pi$ interaction, $n - \pi$ interaction, and hydrogen bond may affect the adsorption capacity of MG.

3.4. Adsorption Kinetics. The kinetics study was carried out at different initial concentration of MG (1000 and 2500 mg/L) and 303 K. In addition, pseudo-first-order (PFO) and pseudo-second-order (PSO) models are used to fit experimental data, and the corresponding model and fitted model parameters of were shown in Figures 8(a)–8(b) and Table S1. It can be seen from the Figure 8(a) that initial adsorption rate was fast, and the initial concentration of MG with 1000 and 2500 mg/L had reached the equilibrium at 80 and 130 min, respectively. This may be because zirconium-based adsorbent has no internal diffusion resistance [19], which makes it easier for MG in aqueous solution to contact with the adsorbent surface, resulting in a fast adsorption rate for MG. The correlation coefficients (R^2) of PSO were greater than PFO by fitting calculation, which indicated that chemisorption was the rate-controlling step of the adsorption process [42].

3.5. Adsorption Isotherms. When the initial MG concentration were the same, the adsorption capacity of MG onto 2.00-ZM adsorbent in 303 K, 313 K, and 323 K condition were evaluated using adsorption isotherms as given in Figures 8(c)–8(e) and stimulated by Langmuir, Freundlich, Temkin, and Sips [43–45] isotherm models. Equation of Sips model is as follow (Langmuir and Freundlich models were shown in Supplementary Information):

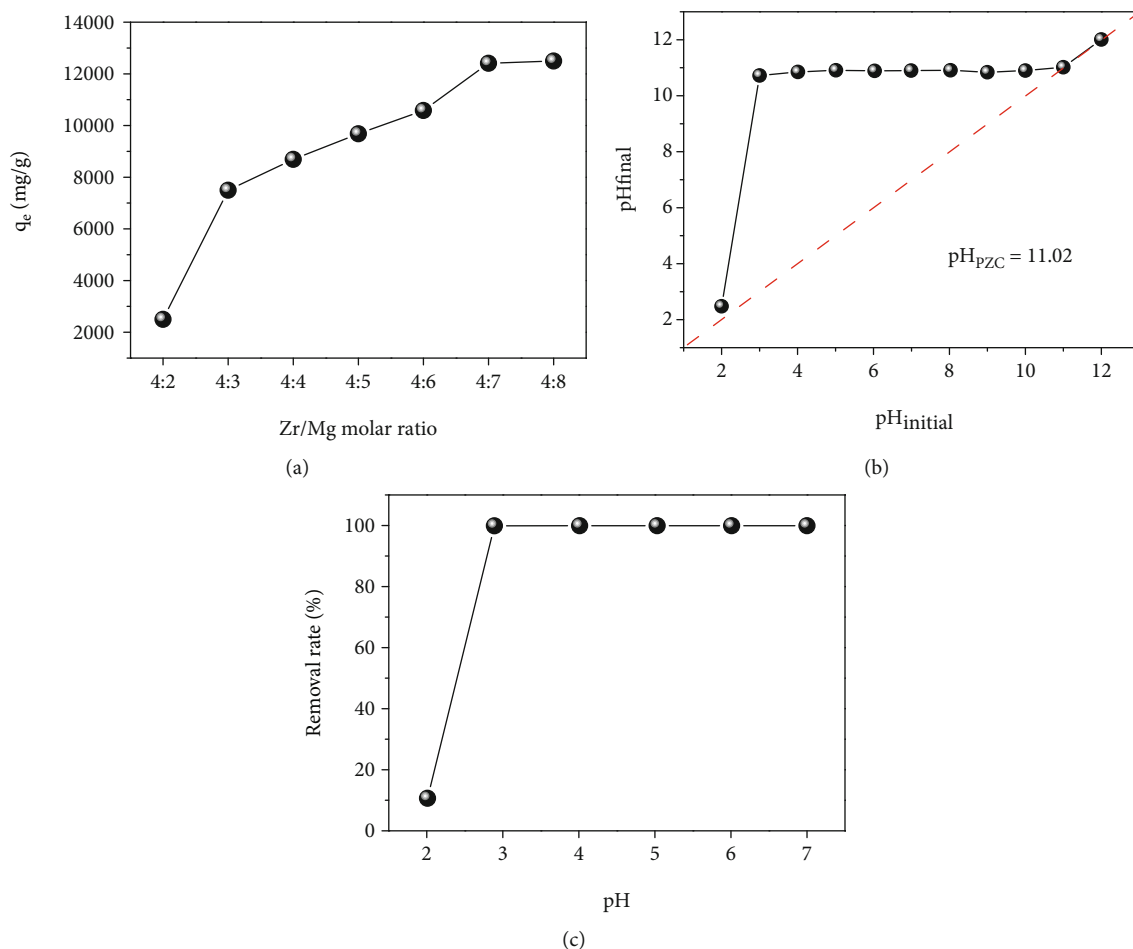$$q_e = \frac{q_m(kc_e)^a}{1 + (kc_e)^a}, \tag{5}$$

(a)

(b)

(c)

FIGURE 6: The adsorbents of different Zr/Mg molar ratio for MG removal (a), pH$_{PZC}$ of the 2.00-ZM (b), and the effect of MG solution (conc.: 1000 mg/L) with different initial pH for 2.00-ZM (c).

where q_m (mg/g) is Sips maximum adsorption capacity, k is the equilibrium constant for heterogeneous solid, and a is the heterogeneous parameter.

It can be seen from Figure 7(a), the adsorption of MG on the surface of 2.00-ZM was hardly affected by temperature when initial MG concentration were same, which indicated that 2.00-ZM has a wide temperature range. In Figure 7(d) and Table S2, these results were shown that three-parameter Sips model was more appropriate to describe adsorption behavior of MG on the 2.00-ZM than the other two classical two-parameter Langmuir and Freundlich models. Which explained that monolayer and multilayer adsorption coexisted in the process of adsorption [46], and the adsorption occurred on heterogeneous surfaces. According to Figures 7(a)–7(d), the equilibrium adsorption capacity increased with the increase of temperature, which demonstrated that MG adsorption on the surface of 2.00-ZM was endothermic. Table 2 presented the comparison of adsorption for MG with other reported adsorbents. It showed that 2.00-ZM is an efficient adsorbent for MG wastewater treatment.

3.6. Adsorption Mechanism. Combined with characterization of y-ZM, adsorption kinetics and isotherms, mechanism of the adsorption process was discussed. The results show that the adsorption mechanism of MG mainly included pore filling, electrostatic attraction, $\pi - \pi$ interaction, and hydrogen bond. Results of N$_2$ adsorption-desorption showed that q_e increased with the increase of pore volume, indicating that pore filling contributed to adsorption. Significant change of -OH of before and after adsorption of 2.00-ZM were observed from FT-IR spectra, suggested that hydrogen bond and $\pi - \pi$ interaction existed between benzene ring in MG molecule and -OH in 2.00-ZM. pH$_{PZC}$ of 2.00-ZM was determined to be 11.02, indicated that the adsorption mechanism of MG involved electrostatic attraction. The possible adsorption mechanism of MG in this adsorption system is shown in Figure 9.

3.7. Reusability of 2.00-ZM. A thermal regeneration method was used to regenerate adsorbent, 0.15 g of used 2.00-ZM was calcined at 600°C for 4 h. The powder collected after cooling to room temperature can be directly used for adsorption experiments. Due to the loss of adsorbents in the process of recovering the adsorbents, the regeneration experiments were carried out according to the proportion of 0.01 g adsorbents used in 25 mL MG solution. The results of the regeneration experiments are shown in Figure 10, and
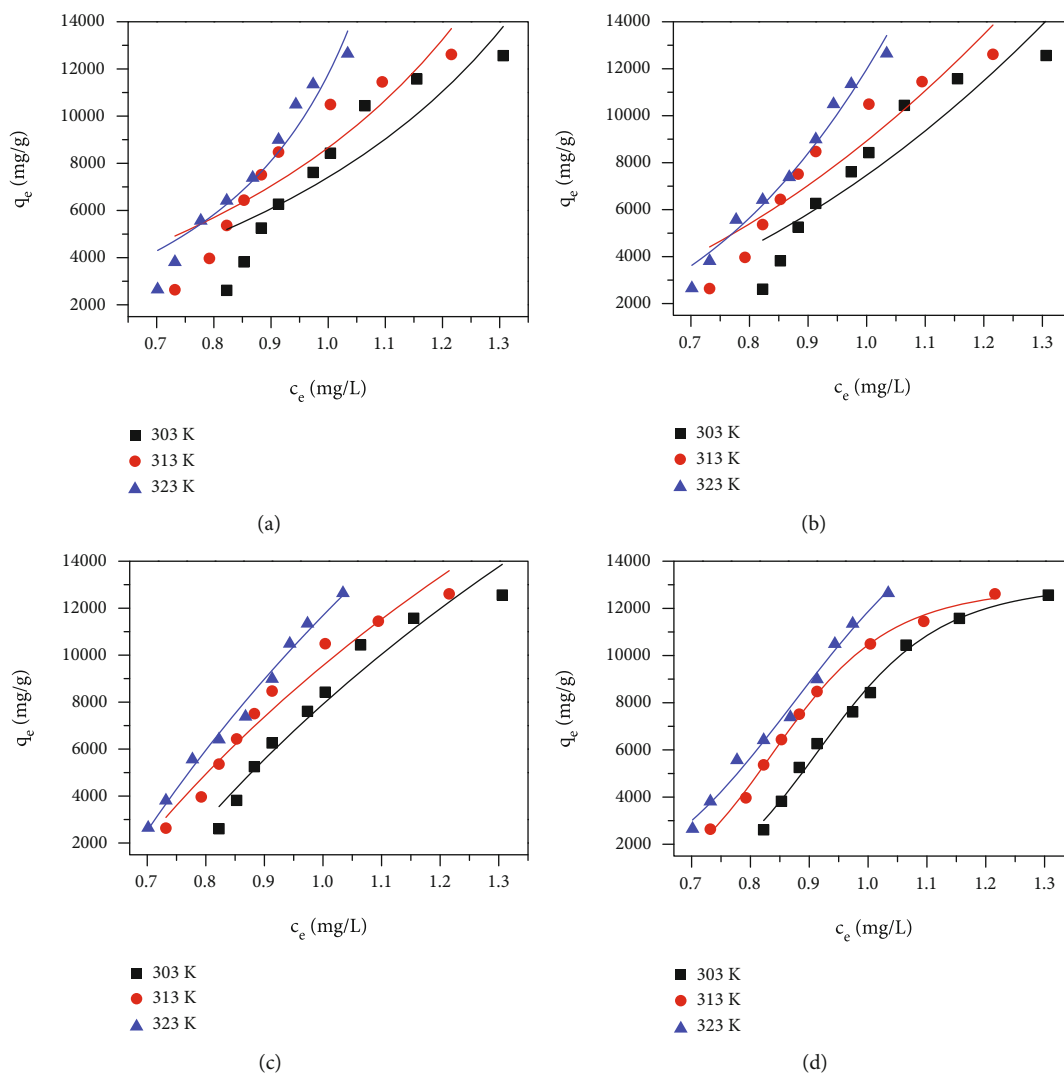
Figure 7: Experimental data fitted with Langmuir (a), Freundlich (b), Temkin (c), and Sips (d) adsorption models for MG adsorption on 2.00-ZM.
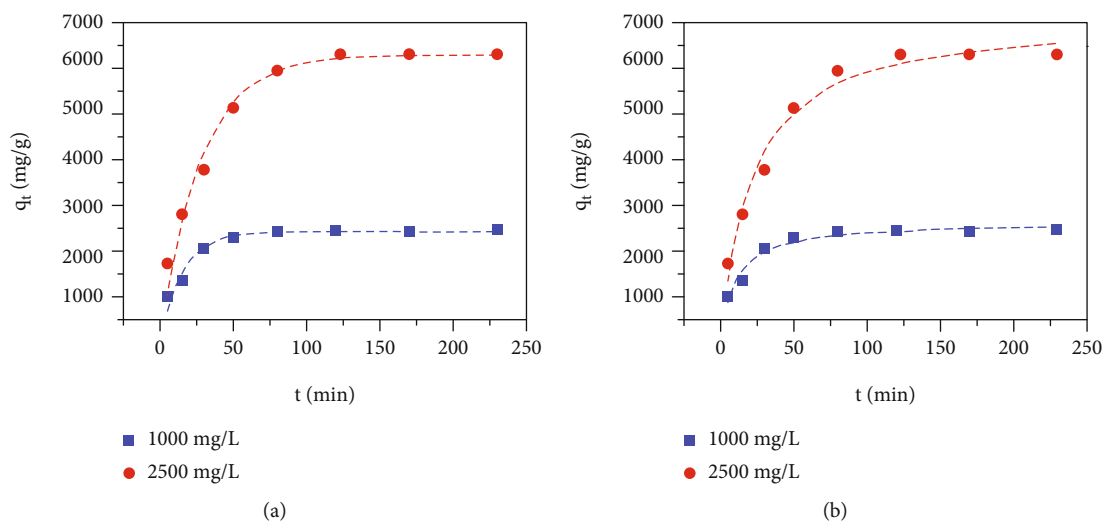

Figure 8: Experimental data fitted with PFO (a) and PSO (b) kinetic models for MG adsorption on 2.00-ZM (solution volume: 450 mL, dose: 0.18 g).

TABLE 2: Comparison of adsorption capacity of 2.00-ZM for MG with other reported adsorbents.

| Adsorbent	q_e (mg/g)	Conditions	Reference
Cross-linked chitosan	714.29	303 K	[47]
N-doped CNTs stabilized Cu_2O	1495.46	pH 4-10	[48]
Chitosan beads	360	296-300K; pH-7	[49]
MgO/Fe_3O_4 nanoparticles	4031.96	318 K	[23]
Magnesium ferrite-doped magnetic biochar	1238.30	298 K	[46]
Activated wakame biochar	4066.96	323 K	[2]
Zeolitic imidazole framework-67	2430	298 K	[6]
Modified rice husk	996.97		[50]
2.00-ZM	12647.60	323 K	This work
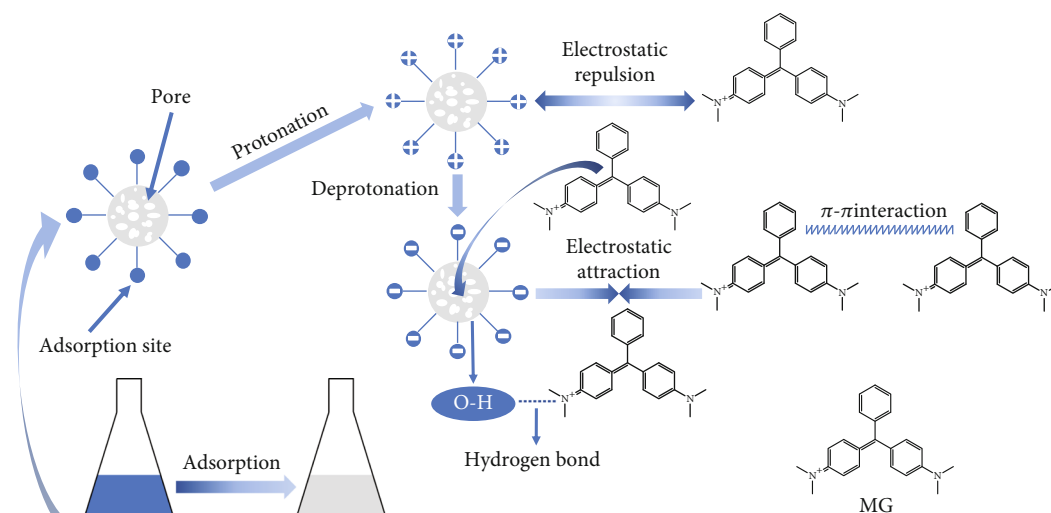
FIGURE 9: Schematic representation of possible adsorption mechanism of MG on the surface of 2.00-ZM.
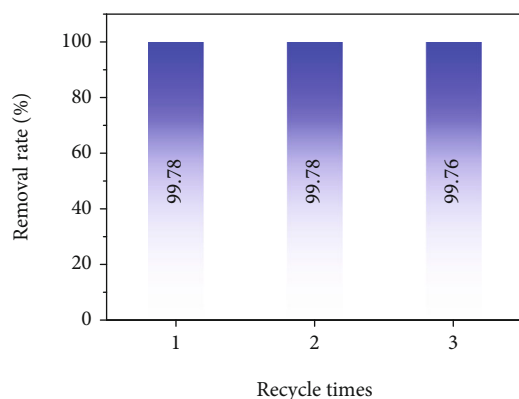

FIGURE 10: Reusability capacity of 2.00-ZM up to three cycles for the removal of MG dye.

the removal rate of MG hardly changed with the increase of the number of cycles. The adsorbent capacity of the adsorbent to MG was more than 99% after three cycles of regeneration. These showed that 2.00-ZM has good regeneration stability, efficient, and promising adsorbent in environmental remediation.

4. Conclusion

Nanoclusters of y-ZM was successfully synthesized by solvothermal method. Characterization of XRD showed that Mg was the main reason for crystalline phase transformation of ZrO_2 from monoclinic to tetragonal phase. Morphology and structure analysis indicated that the series of y-ZM retained nanoclusters structure of ZrO_2, and the lattice fringe of tetragonal ZrO_2 was observed by HR-TEM. Results analysis showed that q_e of the series of y-ZM increased with the increase of Mg abundance and pore volume. Moreover, the optimal 2.00-ZM had a wide pH work range [3–7] and maximum adsorption capacity (12647.60 mg/L). Kinetic analysis showed that the pseudo-second-order kinetic model could obtain better correlation than pseudo-first-order model with kinetic data, and 2.00-ZM can reach 99% removal rate for the initial MG concentration of 2500 mg/L in 130 min. The three-parameter Sips isotherm model had a good correlation coefficient, which indicated that monolayer and multilayer adsorption coexisted in the adsorption process. Pore filling, electrostatic attraction, hydrogen bond, and $\pi - \pi$ interactions were the main factors affecting the adsorption of MG on the 2.00-ZM surface. 2.00-ZM still

maintains a good removal rate for MG after three cycles of regeneration, which demonstrated that the material had high reuse potential and practical application value.

Data Availability

The data used to support the findings of this study are included within the article and Supplementary information files.

Conflicts of Interest

The authors declare that they have no conflicts of interest.

Authors' Contributions

Haoxin Zheng contributed equally to this work and can be considered as co-first authors.

Acknowledgments

Supplementary Materials

Supplementary data associated with this article can be found in the Supplementary Information. *(Supplementary Materials)*

References

[1] A. Meng, J. Xing, Z. Li, and Q. Li, "Cr-doped ZnO nanoparticles: synthesis, characterization, adsorption property, and recyclability," *ACS Applied Materials & Interfaces*, vol. 7, no. 49, pp. 27449–27457, 2015.

[2] X. Yao, L. Ji, J. Guo et al., "An abundant porous biochar material derived from wakame (*Undaria pinnatifida*) with high adsorption performance for three organic dyes," *Bioresource Technology*, vol. 318, article 124082, 2020.

[3] D. Loya-González, M. Loredo-Cancino, E. Soto-Regalado et al., "Optimal activated carbon production from corn pericarp: a life cycle assessment approach," *Journal of Cleaner Production*, vol. 219, pp. 316–325, 2019.

[4] M. T. Yagub, T. K. Sen, S. Afroze, and H. M. Ang, "Dye and its removal from aqueous solution by adsorption: a review," *Advances in Colloid and Interface Science*, vol. 209, pp. 172–184, 2014.

[5] A. A. Alqadami, M. Naushad, Z. A. Alothman, and T. Ahamad, "Adsorptive performance of MOF nanocomposite for methylene blue and malachite green dyes: kinetics, isotherm and mechanism," *Journal of Environmental Management*, vol. 223, pp. 29–36, 2018.

[6] K. Y. Lin and H. A. Chang, "Ultra-high adsorption capacity of zeolitic imidazole framework-67 (ZIF-67) for removal of malachite green from water," *Chemosphere*, vol. 139, pp. 624–631, 2015.

[7] A. Deb, A. Debnath, and B. Saha, "Sono-assisted enhanced adsorption of eriochrome black-T dye onto a novel polymeric nanocomposite: kinetic, isotherm, and response surface methodology optimization," *Journal of Dispersion Science and Technology*, vol. 42, no. 11, pp. 1579–1592, 2021.

[8] S. Chowdhury, R. Mishra, P. Saha, and P. Kushwaha, "Adsorption thermodynamics, kinetics and isosteric heat of adsorption of malachite green onto chemically modified rice husk," *Desalination*, vol. 265, no. 1-3, pp. 159–168, 2011.

[9] A. Mohamed, M. M. Ghobara, M. K. Abdelmaksoud, and G. G. Mohamed, "A novel and highly efficient photocatalytic degradation of malachite green dye via surface modified polyacrylonitrile nanofibers/biogenic silica composite nanofibers," *Separation and Purification Technology*, vol. 210, pp. 935–942, 2019.

[10] N. Joseph, M. A. Mees, M. Vergaelen et al., "Layer-by-layer assembled hydrogen-bonded multilayer poly(2-oxazoline) membranes for aqueous separations," *ACS Applied Polymer Materials*, vol. 2, no. 12, pp. 5398–5405, 2020.

[11] K. Y. Foo and B. H. Hameed, "Insights into the modeling of adsorption isotherm systems," *Chemical Engineering Journal*, vol. 156, no. 1, pp. 2–10, 2010.

[12] L. Bulgariu, L. B. Escudero, O. S. Bello et al., "The utilization of leaf-based adsorbents for dyes removal: a review," *Journal of Molecular Liquids*, vol. 276, pp. 728–747, 2019.

[13] S. Praveen, J. Jegan, T. Bhagavathi Pushpa, R. Gokulan, and L. Bulgariu, "Biochar for removal of dyes in contaminated water: an overview," *Biochar*, vol. 4, no. 1, 2022.

[14] Y. K. Penke, G. Anantharaman, J. Ramkumar, and K. K. Kar, "Aluminum substituted cobalt ferrite (co−Al−Fe) Nano adsorbent for arsenic adsorption in aqueous systems and detailed redox behavior study with XPS," *ACS Applied Materials & Interfaces*, vol. 9, no. 13, pp. 11587–11598, 2017.

[15] B. Saha, A. Debnath, and B. Saha, "Fabrication of PANI@Fe−Mn−Zr hybrid material and assessments in sono-assisted adsorption of methyl red dye: Uptake performance and response surface optimization," *Journal of the Indian Chemical Society*, vol. 99, no. 9, article 100635, 2022.

[16] S. M. M. Amir, M. T. H. Sultan, M. Jawaid et al., "Nondestructive testing method for Kevlar and natural fiber and their hybrid composites," in *Durability and Life Prediction in Biocomposites, Fibre-Reinforced Composites and Hybrid Composites*, pp. 367–388, Elsevier, 2019.

[17] W. Wang, H. Zhang, L. Zhang, H. Wan, S. Zheng, and Z. Xu, "Adsorptive removal of phosphate by magnetic $Fe_3O_4@$," *Colloids and Surfaces A: Physicochemical and Engineering Aspects*, vol. 469, pp. 100–106, 2015.

[18] B. Turan, G. Sarigol, and P. Demircivi, "Adsorption of tetracycline antibiotics using metal and clay embedded cross- linked chitosan," *Materials Chemistry and Physics*, vol. 279, article 125781, 2022.

[19] S. Sonal and B. K. Mishra, "A comprehensive review on the synthesis and performance of different zirconium-based adsorbents for the removal of various water contaminants," *Chemical Engineering Journal*, vol. 424, article 130509, 2021.

[20] R. J. Drout, L. Robison, Z. Chen, T. Islamoglu, and O. K. Farha, "Zirconium metal-organic frameworks for organic pollutant adsorption," *Trends in Chemistry*, vol. 1, no. 3, pp. 304–317, 2019.

[21] J. Hou, H. Wang, and H. Zhang, "Zirconium metal−organic framework materials for efficient ion adsorption and sieving," *Industrial & Engineering Chemistry Research*, vol. 59, no. 29, pp. 12907–12923, 2020.

[22] L. Zhang, P. Hu, J. Wang, and R. Huang, "Adsorption of amido black 10B from aqueous solutions onto Zr (IV) surface-

immobilized cross-linked chitosan/bentonite composite," *Applied Surface Science*, vol. 369, pp. 558–566, 2016.

[23] F. Guo, X. Jiang, X. Li, X. Jia, S. Liang, and L. Qian, "Synthesis of MgO/Fe$_3$O$_4$ nanoparticles embedded activated carbon from biomass for high-efficient adsorption of malachite green," *Materials Chemistry and Physics*, vol. 240, article 122240, 2020.

[24] H. Liu, Z. Mo, L. Li, F. Chen, Q. Wu, and L. Qi, "Efficient removal of copper(II) and malachite green from aqueous solution by magnetic magnesium silicate composite," *Journal of Chemical & Engineering Data*, vol. 62, no. 10, pp. 3036–3042, 2017.

[25] Z. Cui, J. Liu, H. Gao et al., "Size and shape dependences of the adsorption kinetics of malachite green on nano-MgO: a theoretical and experimental study," *Physical Chemistry Chemical Physics*, vol. 21, no. 25, pp. 13721–13729, 2019.

[26] K. C. Das and S. S. Dhar, "Remarkable catalytic degradation of malachite green by zinc supported on hydroxyapatite encapsulated magnesium ferrite (Zn/HAP/MgFe2O4) magnetic novel nanocomposite," *Journal of Materials Science*, vol. 55, no. 11, pp. 4592–4606, 2020.

[27] L. Renuka, K. S. Anantharaju, S. C. Sharma et al., "Hollow microspheres mg-doped ZrO2 nanoparticles: green assisted synthesis and applications in photocatalysis and photoluminescence," *Journal of Alloys and Compounds*, vol. 672, pp. 609–622, 2016.

[28] L. Keerthana, C. Sakthivel, and I. Prabha, "MgO-ZrO$_2$ mixed nanocomposites: fabrication methods and applications," *Materials Today Sustainability*, vol. 3-4, article 100007, 2019.

[29] Z. Li, Y. Sun, J. Xing, Y. Xing, and A. Meng, "One step synthesis of co/Cr-codoped ZnO nanoparticle with superb adsorption properties for various anionic organic pollutants and its regeneration," *Journal of Hazardous Materials*, vol. 352, pp. 204–214, 2018.

[30] H. S. Ramadan, R. A. M. Ali, M. Mobarak et al., "One-step fabrication of a new outstanding rutile TiO2 nanoparticles/anthracite adsorbent: modeling and physicochemical interpretations for malachite green removal," *Chemical Engineering Journal*, vol. 426, article 131890, 2021.

[31] J. S. Noh and J. A. Schwarz, "Estimation of the point of zero charge of simple oxides by mass titration," *Journal of Colloid and Interface Science*, vol. 130, no. 1, pp. 157–164, 1989.

[32] T. Tsoncheva, I. Genova, M. Dimitrov et al., "Nanostructured copper-zirconia composites as catalysts for methanol decomposition," *Applied Catalysis B: Environmental*, vol. 165, pp. 599–610, 2015.

[33] A. B. Nawale, N. S. Kanhe, S. V. Bhoraskar, V. L. Mathe, and A. K. Das, "Influence of crystalline phase and defects in the ZrO$_2$ nanoparticles synthesized by thermal plasma route on its photocatalytic properties," *Materials Research Bulletin*, vol. 47, no. 11, pp. 3432–3439, 2012.

[34] E. X. Ren, D. Y. Wang, Y. T. Li et al., "Thermochemical energy storage drastically enhanced by zirconium oxide and lithium hydroxide for magnesium hydroxide," *Energy Storage*, vol. 4, no. 2, 2022.

[35] Y. Zheng, J. Liu, B. Cheng, W. You, W. Ho, and H. Tang, "Hierarchical porous Al$_2$O$_3$@ZnO core-shell microfibres with excellent adsorption affinity for Congo red molecule," *Applied Surface Science*, vol. 473, pp. 251–260, 2019.

[36] S. F. Wang, F. Gu, M. K. Lü et al., "Structure evolution and photoluminescence properties of ZrO2:Eu^{3+} nanocrystals," *Optical Materials*, vol. 28, no. 10, pp. 1222–1226, 2006.

[37] N. Zeeshan and Rafiuddin, "Solid electrolytes based on {1 − (x + y)}ZrO$_2$-(x)MgO-(y)CaO ternary system: preparation, characterization, ionic conductivity, and dielectric properties," *Journal of Advanced Research*, vol. 9, pp. 35–41, 2018.

[38] L. A. Pérez-Maqueda and E. Matijević, "Preparation and characterization of nanosized zirconium (hydrous) oxide particles," *Journal of Materials Research*, vol. 12, no. 12, pp. 3286–3292, 1997.

[39] J. G. S. van Jaarsveld, J. S. J. van Deventer, and G. C. Lukey, "The effect of composition and temperature on the properties of fly ash- and kaolinite-based geopolymers," *Chemical Engineering Journal*, vol. 89, no. 1-3, pp. 63–73, 2002.

[40] H. Yang, Y. Sun, Q. Zhang et al., "ZrMOX particles for enhanced removal of methyl orange from wastewater: preparation, characterization, and adsorption study," *Adsorption Science & Technology*, vol. 2022, article 9685352, pp. 1–11, 2022.

[41] M. A. Ahmad and R. Alrozi, "Removal of malachite green dye from aqueous solution using rambutan peel-based activated carbon: equilibrium, kinetic and thermodynamic studies," *Chemical Engineering Journal*, vol. 171, no. 2, pp. 510–516, 2011.

[42] S. Dutta, S. K. Srivastava, B. Gupta, and A. K. Gupta, "Hollow polyaniline microsphere/MnO2/Fe3O4 nanocomposites in adsorptive removal of toxic dyes from contaminated water," *ACS Applied Materials & Interfaces*, vol. 13, no. 45, pp. 54324–54338, 2021.

[43] G. P. Jeppu and T. P. Clement, "A modified Langmuir-Freundlich isotherm model for simulating pH-dependent adsorption effects," *Journal of Contaminant Hydrology*, vol. 129-130, pp. 46–53, 2012.

[44] R. A. Koble and T. E. Corrigan, "Adsorption isotherms for pure hydrocarbons," *Industrial and Engineering Chemistry*, vol. 44, no. 2, pp. 383–387, 1952.

[45] N. Ayawei, A. N. Ebelegi, and D. Wankasi, "Modelling and interpretation of adsorption isotherms," *Journal of Chemistry*, vol. 2017, Article ID 3039817, 11 pages, 2017.

[46] Q. Wen, Y. Chen, X. Rao et al., "Preparation of magnesium ferrite-doped magnetic biochar using potassium ferrate and seawater mineral at low temperature for removal of cationic pollutants," *Bioresource Technology*, vol. 350, article 126860, 2022.

[47] R. Chanajaree, M. Sriuttha, V. S. Lee, and K. Wittayanarakul, "Thermodynamics and kinetics of cationic/anionic dyes adsorption on cross- linked chitosan," *Journal of Molecular Liquids*, vol. 322, article 114507, 2021.

[48] X. Li, Y. Zhang, L. Jing, and X. He, "Novel N-doped CNTs stabilized Cu2O nanoparticles as adsorbent for enhancing removal of malachite green and tetrabromobisphenol a," *Chemical Engineering Journal*, vol. 292, pp. 326–339, 2016.

[49] D. Das and A. Pal, "Adsolubilization phenomenon perceived in chitosan beads leading to a fast and enhanced malachite green removal," *Chemical Engineering Journal*, vol. 290, pp. 371–380, 2016.

[50] X. You, R. Zhou, Y. Zhu, D. Bu, and D. Cheng, "Adsorption of dyes methyl violet and malachite green from aqueous solution on multi-step modified rice husk powder in single and binary systems: characterization, adsorption behavior and physical interpretations," *Journal of Hazardous Materials*, vol. 430, article 128445, 2022.